https://doi.org/10.5194/egusphere-2025-6357
Preprint. Discussion started: 29 January 2026

High-resolution monthly glacier surface velocity mapping in the Kangri Karpo region (2015–2024) using multi-source remote sensing data fusion

Daoxun Gao[1,2,3,4], Kunpeng Wu[1,2], Yunpeng Duan[1,2,3,4], Zhaoqi Ji[1,2,3,4], Danyu Ma[1,2,3,4], Tobias Bolch[5], Cheng Huang[6], Shiyin Liu[1]

[1]Institute of International Rivers and Eco-Security, Yunnan University, Kunming 650091, China
[2]Yunnan Key Laboratory of International Rivers and Transboundary Eco-security, Yunnan University, Kunming 650091, China
[3]Ministry of Education Key Laboratory for Transboundary Eco-Security of Southwest China, Yunnan University, Kunming 650091, China
[4]Yunnan International Joint Laboratory of China-Laos-Bangladesh-Myanmar Natural Resources Remote Sensing Monitoring, Yunnan University, Kunming 650091, Yunnan, China
[5]Institute of Geodesy, Graz University of Technology, Graz, Austria
[6]Yunnan Geological Environment Monitoring Institute, Kunming 650216, Yunnan, China

Correspondence to: Kunpeng Wu (wukunpeng@ynu.edu.cn)

Abstract. To improve the accuracy and timeliness of glacier surface-velocity retrieval in complex mountain terrain, we develop a high-resolution fusion method combining Landsat, Sentinel-1/2, and UAV (Unmanned Aerial Vehicle) data, and produce monthly velocity products for the Kangri Karpo region for 2015–2024. Compared with existing large-area public datasets, the products offer markedly higher spatial resolution and better detection of small mountain glaciers; relative to single-sensor inputs prior to fusion, the valid-pixel ratio increases by ~50%, the average number of valid months per pixel over the decade rises by ~50, and spatial smoothness improves—demonstrating the method's suitability for rugged terrain. Spatially, velocities follow the canonical "fast center, slow margins" pattern, with multi-year maxima >700 $m \cdot yr^{-1}$ and values in lower reaches and most tributaries generally <100 $m \cdot yr^{-1}$. Attribute analysis indicates significant correlations between velocity and area, slope, and aspect: larger glaciers flow faster overall; within individual glaciers, velocity responds more strongly to slope; after controlling for area and slope, south-facing glaciers are slightly faster. Temporally, the intra-annual series shows clear seasonality, with peaks at the beginning and end of the melt season and sustained high speeds throughout. At the interannual scale, most pixelwise decadal trends lie within −0.1 to +0.1 $m \cdot d^{-1} \cdot dec^{-1}$ (overall subdued change), and the median trend is slightly positive, indicating weak regional acceleration; ~38.3% of glaciers accelerate significantly, 25.5% decelerate significantly, and 36.2% show no significant trend ($p \geq 0.05$). By aspect, significant acceleration is concentrated on south- and west-facing glaciers, whereas significant deceleration occurs mainly on east- and north-facing glaciers. Month-resolved trends indicate acceleration primarily in April–May (~0.15–0.20 $m \cdot d^{-1} \cdot dec^{-1}$), likely linked to enhanced meltwater input from an advanced melt season, and deceleration concentrated in July–August (≤ −0.15 $m \cdot d^{-1} \cdot dec^{-1}$), plausibly associated with intensified mass deficit.

https://doi.org/10.5194/egusphere-2025-6357
Preprint. Discussion started: 29 January 2026

1 Introduction

The cryosphere is an integral component of Earth's climate system, encompassing ice sheets, glaciers, permafrost, seasonal snow, and sea ice, and it serves as a key indicator and regulator of global climate change (Slaymaker and Kelly, 2007). As a major subsystem of the cryosphere, glaciers are both principal reservoirs of global freshwater and highly sensitive to warming; their retreat and accelerated melt exert far-reaching impacts by altering the hydrological cycle, modulating atmospheric circulation, and driving sea-level rise (Huss and Hock, 2015; Zemp et al., 2019). Evidence shows that glacier mass loss is now among the leading contributors to global sea-level rise (Ren et al., 2011; Liu et al., 2021), and its evolution affects regional water security while playing a significant role in climate-system feedbacks (Fountain et al., 2012).

Within the global glacier system, mountain glaciers account for only a small share of total ice storage but respond more sensitively to climatic perturbations (Zhang et al., 2015; Chen et al., 2019). Their meltwater directly shapes the spatiotemporal distribution of downstream runoff and underpins ecosystem stability (Slemmons et al., 2013; Zhang et al., 2020). In mid- to low-latitude, high-elevation regions such as the Qinghai–Tibet Plateau, glacier change not only governs headwater hydrology (Nan et al., 2025; Yao et al., 2023) but also has far-reaching implications for agriculture, ecosystems, and disaster-risk management (Zhang et al., 2007; Zhang et al., 2020). Consequently, sustained, fine-resolution monitoring of mountain-glacier change is foundational for regional water-resource assessments and studies of climate responses (Zongxing et al., 2016).

Among the available indicators, glacier surface velocity is the central metric linking ice dynamics and mass balance. It captures the mechanical regulation of ice flow and associated energy-mass transfers, offering direct utility for diagnosing climate-forced dynamic responses, assessing downstream hydrologic risk, and characterizing glacier–climate coupling (Luckman et al., 2003; Huang and Li, 2011). Traditional in-situ techniques (e.g., theodolite, total station, GPS stake methods) yield high-accuracy point measurements but are constrained by high-elevation conditions, limited accessibility, and labor costs, impeding sustained, basin- to region-scale monitoring (Yan et al., 2015). By contrast, remote sensing—non-contact, synoptic, and repeatable—has become the primary approach for velocity monitoring (Luckman et al., 2007; Fan et al., 2019; Fu et al., 2022). Recent advances in multi-source data fusion and state-of-the-art algorithms have markedly improved the spatiotemporal resolution of velocity retrievals, strengthening our capacity to resolve dynamical evolution and its climatic drivers (Wang et al., 2019; Mohanty et al., 2025).

Located at the eastern terminus of the Nyainqêntanglha Range in the southeastern Qinghai – Tibet Plateau, the Kangri Karpo region is one of the Plateau's most humid, maritime-glacier clusters, strongly influenced by the Indian monsoon, with elevations ranging from ~2,400 to 6,600 m (Wu et al., 2021). Glacier area and volume there have changed markedly over recent decades. In 2015, the total glacierized area was approximately 2,048.50 ± 48.65 km² (Wu et al., 2021), whereas in the 1980s it reached 2,655.2 km² (Wu et al., 2018). This implies a reduction of about 679.51 ± 59.49 km²—roughly 24.9% of the

https://doi.org/10.5194/egusphere-2025-6357
Preprint. Discussion started: 29 January 2026

total area—over the past three-plus decades (Wu et al., 2018), underscoring the region's pronounced sensitivity to climate change.

At present, no dedicated glacier surface-velocity dataset exists for the Kangri Karpo region. Global products that cover the area include: (i) GoLIVE (Global Land Ice Velocity Extraction from Landsat 8), derived from Landsat OLI imagery using the Python Correlation (PyCorr) image cross-correlation workflow, spanning 1 May 2013 to 30 April 2017 with a 16-day temporal resolution and 300 m × 300 m spatial resolution (Fahnestock et al., 2016; Lei et al., 2021); and (ii) ITS_LIVE (Inter-mission Time Series of Land Ice Velocity and Elevation), produced with autoRIFT (autonomous Repeat Image Feature Tracking) from Landsat 4/5/7/8 imagery under NASA's MEaSUREs program, covering glaciers larger than 5 km² from 12 November 1982 to 27 April 2019, with temporal resolution of 6-546 days and 240 m × 240 m spatial resolution (Gardner et al., 2018). Both datasets are available from the National Snow and Ice Data Center. However, these products have notable limitations: (1) relatively coarse spatial resolution, which hampers characterization of fine-scale velocity heterogeneity; (2) discontinued updates, limiting near-real-time monitoring and long-term trend analyses for recent years; and (3) substantial data gaps (NoData), which reduce completeness and reliability and complicate analysis. In sum, high-resolution glacier surface-velocity products remain scarce for the Kangri Karpo region.

The Kangri Karpo region features rugged relief and persistent cloud cover, which pose substantial challenges for remotely sensing glacier surface velocity. Optical sensors offer high spatial resolution but are strongly affected by clouds and seasonal snow, limiting temporal coverage and data usability (Scherler et al., 2008; Berthier et al., 2005). Radar sensors operate in all weather and penetrate clouds, yet mountainous terrain induces layover, shadowing, and geometric distortions, leading to spatial data gaps (Kääb et al., 2005; Zhou et al., 2014). Consequently, fusing optical and radar observations provides complementary strengths in spatiotemporal resolution, observational completeness, and robustness, markedly improving the continuity and accuracy of velocity monitoring (Fan et al., 2019; Mohanty et al., 2025; Ye et al., 2024; Maksymiuk et al., 2016). This multi-source integration has become a key research direction for complex mountain-glacier environments, including the southwestern Tibetan Plateau.

Motivated by these limitations, this study develops a multi-sensor glacier surface-velocity product for the Kangri Karpo region. We perform weighted fusion of velocities derived from Landsat OLI, Sentinel-1 GRD, and Sentinel-2 MSI imagery to generate a high-spatiotemporal-resolution dataset for 2015–2024. We then examine spatiotemporal variability at decadal and seasonal scales to characterize glacier dynamics across the region, providing new support for glacier-velocity research in southeastern Tibet.

2 Study area

Located at the eastern terminus of the Nyainqêntanglha Range on the southeastern Qinghai – Tibet Plateau, the Kangri Karpo region is among the Plateau's wettest sectors (Wu et al., 2021). It spans 29°00′ – 29°30′ N and 96°20′ – 97°10′ E, with elevations from ~2,400 to 6,600 m.

https://doi.org/10.5194/egusphere-2025-6357
Preprint. Discussion started: 29 January 2026

Climatically, the area lies within the monsoonal temperate glacier region and is strongly influenced by the Indian monsoon, resulting in high annual precipitation and humidity (Yang et al., 2008). Owing to recent warming, glacier area and volume have declined markedly over recent decades, with signs of accelerated ablation. Given the region's complex climatic setting, Kangri Karpo glaciers exhibit pronounced sensitivity to climate variability, and their dynamics closely track local atmospheric fluctuations (Wu et al., 2021).

Glaciers are widely distributed across the massif. According to RGI 7.0, the region contains 218 glaciers (Figure 1): 162 smaller than 1 km², 30 between 1 and 5 km², and 26 larger than 5 km². Among the largest, the Yanong and Xirinongpu glaciers have surface areas of approximately 165 km² and 94 km², respectively (RGI Consortium, 2023).

Beyond its climatic significance, Kangri Karpo is a key region for understanding glacier change across the Qinghai–Tibet Plateau. Continued retreat is likely to affect local ecosystems, water-resources management, and livelihoods. Long-term monitoring and analysis are therefore essential for anticipating future water-supply shifts and informing strategies to adapt to climate change.

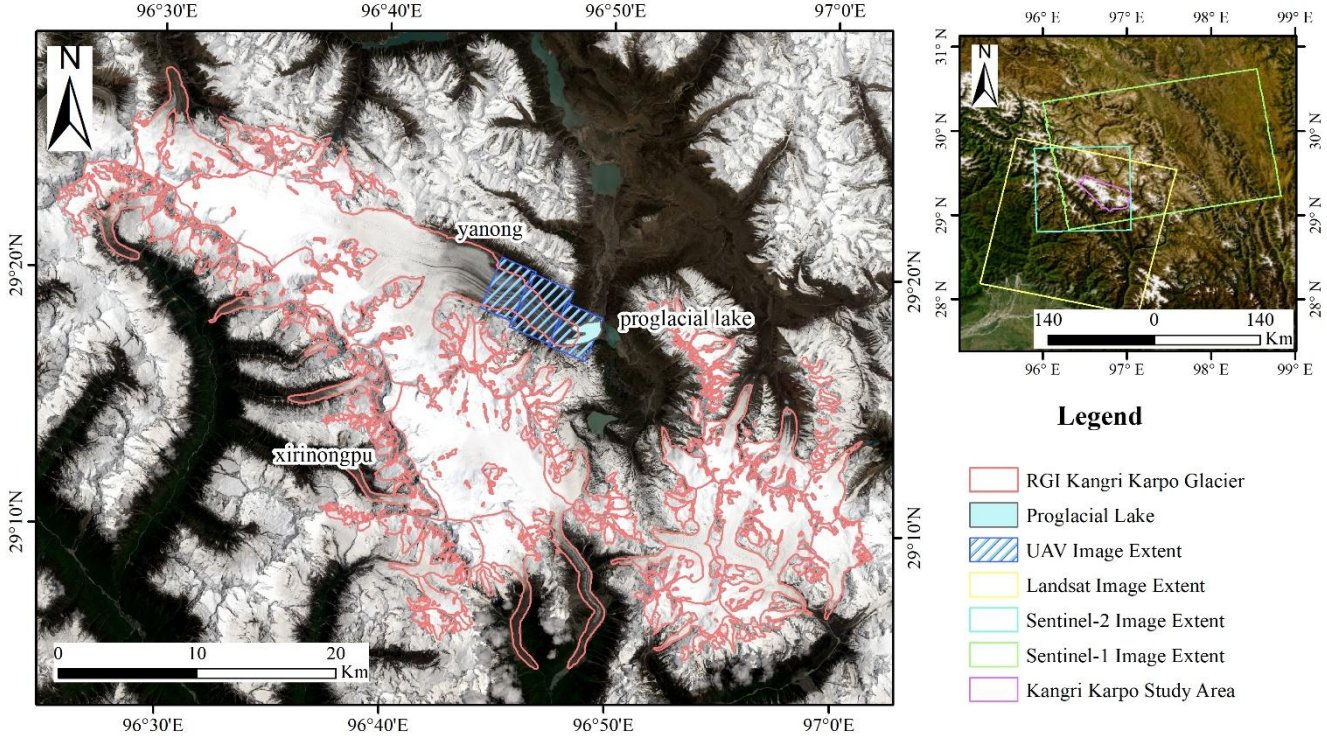

Figure 1: Study area of the Kangri Karpo region. Background: true colour image from Landsat 8/9 Collection 2 Level-1 (scene ID LC09_L1TP_134040_20230902_20230902_02_T1; acquired 2 September 2023), courtesy of the USGS (https://glovis.usgs.gov, last access: 11 September 2025). Inset (upper-right panel): Esri World Imagery (https://www.arcgis.com, last access: 11 September 2025).

https://doi.org/10.5194/egusphere-2025-6357
Preprint. Discussion started: 29 January 2026

3 Materials and methods

3.1 General workflow

To obtain a high spatiotemporal resolution glacier surface-velocity product for the Kangri Karpo region (monthly, 30 m), we designed a workflow centered on multi-sensor data fusion. The rationale is to exploit the complementarity of optical and radar observations: first retrieve displacements/velocities for each sensor stream using robust methods, then estimate fusion weights and repair gaps to produce a spatially consistent monthly field, followed by uncertainty quantification and spatiotemporal analyses.

Key steps are as follows:(1) Image pairing and preprocessing: Assemble monthly image pairs from Landsat-8/9 OLI and Sentinel-2 MSI (optical) and Sentinel-1 IW GRD (radar); perform geometric co-registration and basic correct(2) Optical velocity retrieval: Apply frequency-domain phase correlation (COSI-Corr) for feature matching; derive east–west (E–W) and north–south (N–S) displacements and convert them to daily-mean speeds.(3) Radar velocity retrieval: Use intensity-based pixel-offset tracking on Sentinel-1 to estimate range/azimuth offsets and convert to speed, providing stable coverage under cloudy conditions.(4) Temporal robustification and quality control: Remove mismatches using signal-to-noise ratio (SNR) and robust time-series filtering to ensure cross-sensor consistency and reliability.(5) Weighted least-squares fusion (WLS): With co-temporal UAV-derived velocities as reference, estimate optimal weights for optical and radar fields and fuse them on a common grid, yielding a monthly product with fewer gaps and reduced noise.(6) Local enhancement-factor gap filling: For residual voids, construct a Sentinel-1-guided enhancement-factor field to infill and smooth, improving spatiotemporal continuity.(7) Fusion evaluation and spatiotemporal analysis: Assess fusion performance using multiple diagnostics, quantify uncertainties, and analyze decadal and seasonal variability using the fused series.

The complete workflow is illustrated in Figure 2.

https://doi.org/10.5194/egusphere-2025-6357
Preprint. Discussion started: 29 January 2026

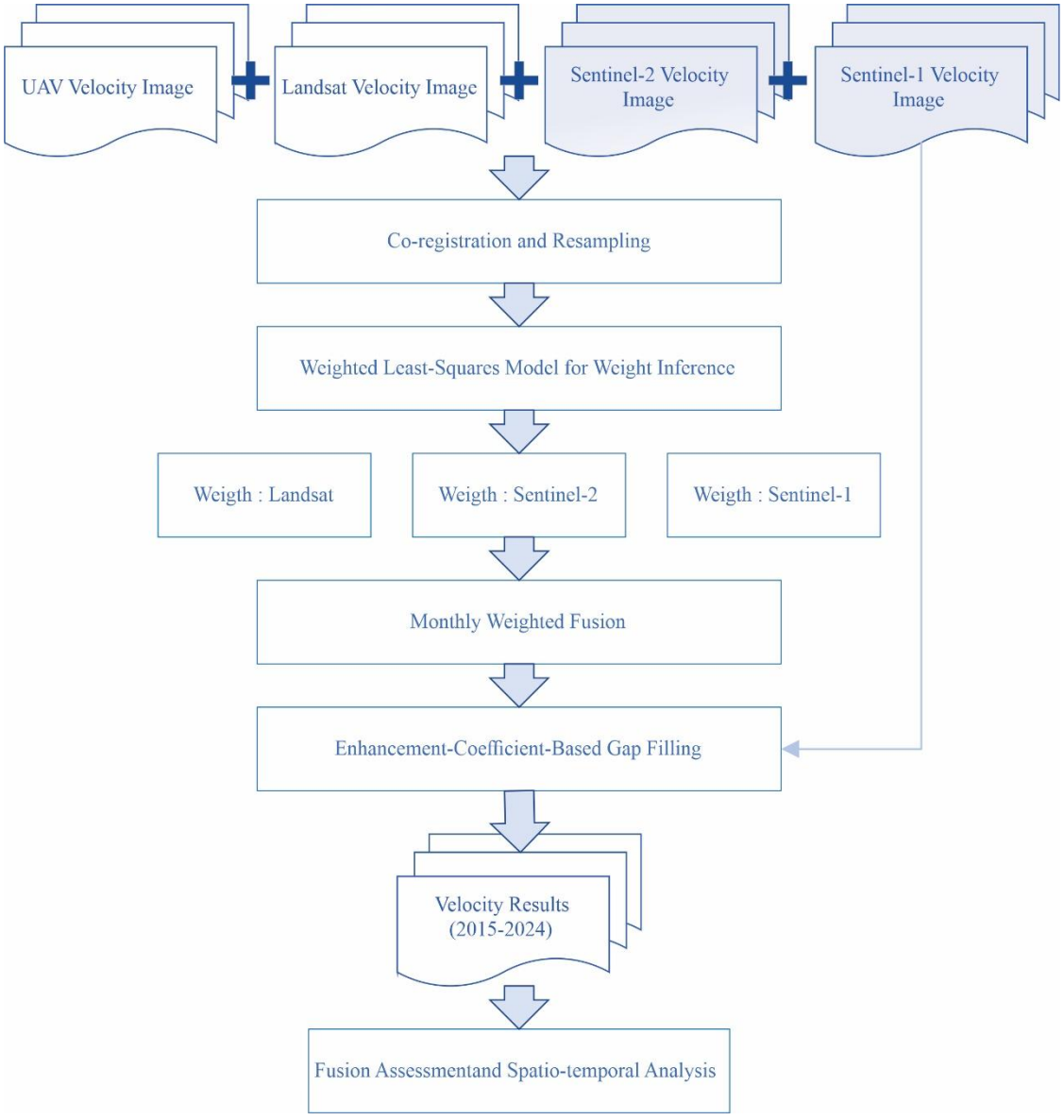

Figure 2: Workflow of this study. Input datasets and outputs are shown in gradient blue; processing and analysis steps are shown in white.

3.2 Imagery selection

For Landsat OLI imagery, we used Band 8 (panchromatic; 15 m). Scenes were downloaded from the USGS (http://glovis.usgs.gov) as Collection-2 Level-1 products, which are system-corrected and directly suitable for analysis. To

https://doi.org/10.5194/egusphere-2025-6357
Preprint. Discussion started: 29 January 2026

approximate a monthly product, we preferentially selected low-cloud scenes and paired acquisitions from the beginning and end of each month. Given the frequent cloud cover over high mountains, some months required extending the pairwise time interval to mitigate cloud contamination. The detailed information on the Landsat imagery used in this study is provided in Table S1 of the Supplementary Material.

For Sentinel-1, we used Interferometric Wide (IW) mode, Ground Range Detected (GRD) scenes. To target a monthly cadence, we paired images near month start and end; because Sentinel-1A has a 12-day revisit, monthly coverage is not exact, and most pairs have temporal baselines of 24 or 36 days. All scenes were obtained from the Copernicus Data Space Browser(https://browser.dataspace.copernicus.eu). The detailed information on the Sentinel-1 imagery used in this study is provided in Table S2 of the Supplementary Material.

For Sentinel-2 MSI, we used Band 8 (near-infrared; 10 m) from Level-1C products, which are geometrically corrected and usable as is. Data were downloaded from the same Copernicus portal, and the selection criteria matched those for Landsat (low cloud, early/late-month pairing). The detailed information on the Sentinel-2 imagery used in this study is provided in Table S3 of the Supplementary Material.

In addition, we acquired UAV photogrammetry for reference and evaluation using a DJI Matrice 300 RTK equipped with a M6 Pro (M6P) metric mapping camera. Six orthomosaics were collected in June-November 2023, forming five image pairs. Although coverage is limited to ~30 km² near the Yanong Glacier terminus, the area exhibits high flow speeds and diverse surface types (bare ice and debris-covered ice), providing representative conditions for assessing sensor performance. Because error characteristics within a given sensor vary modestly across the region, we use fusion weights calibrated in this subset to parameterize the basin-wide fusion, ensuring practical applicability at regional scale.

3.3 Glacier surface velocity calculation

For Landsat and Sentinel-2 imagery, velocities were derived with COSI-Corr using a frequency-domain cross-correlation algorithm. The search window was 32*32 pixels; the step size was 2 pixels for Landsat OLI and 3 pixels for Sentinel-2 MSI; the correlation threshold was 0.95. East-west (E-W) and north-south (N-S) displacements were combined to form total displacement, which was then divided by the pairwise time baseline to obtain monthly glacier surface speeds at 30 m resolution.

To enhance reliability, we first removed mismatches with speeds > 3 m d^{-1} and low-confidence pixels with SNR < 0.9. We then applied an intra-annual α-trimmed mean filter to stabilize each pixel's time series. Specifically, for each pixel we collected the 12 monthly speeds within a year, set $\alpha = 0.33$, discarded the lowest and highest 33% of ranked values, and averaged the central 34% (quantiles 0.33-0.67) to obtain a year-representative reference map. Monthly maps were compared to this reference on a per-pixel basis; values exceeding 1.5* or falling below 0.5* the reference were flagged as outliers and removed. The SNR screening combined with the time-series filter yielded high-quality monthly velocity fields at 30 m, suitable for subsequent fusion.

https://doi.org/10.5194/egusphere-2025-6357
Preprint. Discussion started: 29 January 2026

For Sentinel-1 GRD data, speeds were computed with SNAP's offset-tracking, using 128-pixel square matching windows and a correlation threshold of 0.95; results were resampled to 30 m. UAV-based glacier velocities were extracted with the ImGRAFT toolbox and likewise resampled to 30 m for estimating fusion weights.

3.4 Data fusion

This study adopts a multi-sensor image-fusion approach to glacier surface velocity, leveraging the complementary strengths of Landsat, Sentinel-1, and Sentinel-2 to produce monthly 30-m products with fewer gaps and improved temporal continuity. The method comprises three stages: estimation of fusion weights, weighted fusion, and enhancement-based gap repair.

First, monthly velocity fields are generated independently from Landsat, Sentinel-1, and Sentinel-2 imagery using cross-correlation. Co-temporal UAV orthomosaics are then processed via cross-correlation to obtain high-accuracy velocities, which are treated as the period's reference ("truth"). Using the three satellite velocity maps and the UAV reference for the same period, we formulate a weighted least-squares (WLS) fit to estimate the optimal fusion weights for the three data sources.

Let $V_{\text{uav}}(i,j)$ denote the UAV-derived velocity at pixel (i,j), and $L(i,j)$,$S_1(i,j)$,$S_2(i,j)$ denote the Landsat, Sentinel-1, and Sentinel-2 velocities, with corresponding fusion weights w_L, w_{S1}, w_{S2}. The WLS objective is:

$$f(w) = \sum_{i=1}^{n} \left[V_{\text{uav}}(i,j) - \left(w_L \cdot L(i,j) + w_{S1} \cdot S_1(i,j) + w_{S2} \cdot S_2(i,j)\right)\right]^2 \quad (1)$$

After setting the partial derivatives of the objective with respect to each weight to zero, the normal equations yield the optimal weight triplet. These weights are then applied to fuse the remaining monthly velocity maps.

In the fusion stage, to address pixels with missing values (NoData), we introduce a binary mask $M_k(i,j)$ to locally renormalize the weights, so that the weighted average at (i,j) is computed only over sources that are valid there (Landsat or Sentinel-2). The preliminary fused velocity is:

$$F(i,j) = \frac{w_{S1} \cdot S_1(i,j) \cdot M_{S1}(i,j) + w_{S2} \cdot S_2(i,j) \cdot M_{S2}(i,j) + w_L \cdot L(i,j) \cdot M_L(i,j)}{w_{S1} \cdot M_{S1}(i,j) + w_{S2} \cdot M_{S2}(i,j) + w_L \cdot M_L(i,j)} \quad (2)$$

Although weighted fusion can effectively integrate multi-source information, some areas may still contain NoData. To further fill these gaps and enhance data continuity, this study introduces a sliding window enhancement-coefficient infilling method. This method uses Sentinel-1 data to infer the spatial variation of the fused values and fills NoData accordingly. Specifically, within a 10*10-pixel sliding window Ω (stride = 5 pixels), an enhancement coefficient a_Ω is defined to represent the response of the fused value to Sentinel-1, with the estimation formula given as:

$$a_\Omega = \frac{\sum_{(i,j)\in\Omega} F(i,j) \cdot S_1(i,j)}{\sum_{(i,j)\in\Omega} S_1(i,j)^2} \quad (3)$$

https://doi.org/10.5194/egusphere-2025-6357
Preprint. Discussion started: 29 January 2026

Only pixels where both $F(i,j)$ and $S_1(i,j)$ are valid are included in the summation. Next, the enhancement-coefficient field a_Ω over the entire image is smoothed with a Gaussian filter to improve spatial continuity. Finally, for missing pixels (i,j) in the fused image, infilling is performed using the following expression:

$$F_{filled}(i,j) = \begin{cases} F(i,j), if\ F(i,j)\ is\ valid \\ a_\Omega \cdot S_1(i,j), if\ F(i,j) = Nodata \end{cases} \quad (4)$$

Through this enhancement-based infilling, the spatial completeness of the fused image is markedly improved and gaps are reasonably reconstructed, providing more stable and continuous data support for subsequent glacier-change analyses and time-series modeling.

3.5 Fusion performance assessment

To comprehensively assess the effectiveness of the fusion method in improving glacier surface-velocity image quality, we designed several experiments as follows.

We selected the two largest glaciers in the study area-Yanong Glacier and Xirinongpu Glacier-as representative test sites because of their large areas, intact morphology, well-defined boundaries, and good data coverage, which together provide strong representativeness for evaluating the method's adaptability and gains under different glacier conditions.

To visualize quality changes before and after fusion, we compared the fused results with velocities from two mainstream optical sources-Landsat and Sentinel-2-separately. Both are widely used for velocity retrieval but are limited by long revisit (Landsat) and heavy cloud interference (Sentinel-2). Such contrasts verify whether fusion effectively integrates strengths and mitigates weaknesses. Note that although Sentinel-1 SAR is included, it is not contrasted separately: (i) it mainly supplements optical data during cloudy seasons and has limited accuracy in steep, deeply incised terrain; and (ii) within our framework its weight is low (≈0.08) and further modulated by the enhancement-coefficient field, yielding a small contribution to final quality. Accordingly, this section focuses on before–after comparisons for Landsat and Sentinel-2 to highlight systematic improvements to the primary observations.

The experiments evaluate improvements in three aspects-spatial completeness, temporal availability, and image smoothness.(1) Spatial completeness: For monthly rasters (2015–2024) of Landsat, Sentinel-2, and the fused product, we compute the valid-pixel ratio within the analysis mask (valid pixels / total pixels), compare coverage, and calculate the fusion improvement rate.(2) Temporal availability: Using per-pixel monthly validity over 2015–2024 (120 months), we count usable months for each pixel to form before-after comparisons.(3) Image smoothness: For the three velocity products and for GoLIVE and ITS_LIVE, we compute the pixelwise standard deviation within the mask for each month. Changes in standard deviation indicate noise suppression and smoothing, enabling a comprehensive assessment of fusion-driven gains in coverage, temporal continuity, and smoothness.

https://doi.org/10.5194/egusphere-2025-6357
Preprint. Discussion started: 29 January 2026

3.6 Uncertainty analysis

Given the limited temporal coverage of available reference velocity products, which precludes their use as accuracy benchmarks over the full study period, we conduct an uncertainty analysis using indirect metrics based on the fused data's internal consistency and stability. Considering the scarcity of long, continuous ground observations in high-mountain regions, we employ a stable-area velocity-fluctuation method, constructing an error model in topographically stable, snow-/ice-free zones surrounding the glaciers to indirectly evaluate the velocity uncertainty of different products.

The basic assumption is that, in stable bare-rock areas outside glaciers, the surface exhibits no significant deformation or displacement, so the true velocity can be approximated as zero. Thus, velocities observed by a product in these areas can be treated as error, and their variability reflects the product's intrinsic uncertainty. The velocity error E_{off} is estimated as follows:

$$E_{\text{off}} = \sqrt{E_m^2 + E_s^2} \tag{5}$$

Where E_m denotes the mean pixel velocity within the stable area, reflecting systematic bias; E_s is the standard error of the velocities, characterizing random noise, given by:

$$E_s = \frac{\sigma}{\sqrt{N_e}} \tag{6}$$

Where σ denotes the standard deviation of velocities within the stable area, and N_e is the effective number of independent pixels after accounting for spatial autocorrelation; its computation is as follows:

$$N_e = \frac{N_t \times R}{2D} \tag{7}$$

In the equation, N_t denotes the total number of valid velocity pixels within the stable area; R is the image spatial resolution (m); and (D) is the spatial autocorrelation distance. Following Sun et al. (2017), D can be approximated as 20 times the pixel size. Accordingly, by computing E_{off} in stable areas for different velocity products, we can conduct a cross-comparison under a common standard among Landsat, Sentinel-2, the fused result, ITS_LIVE, and GoLIVE, thereby evaluating the practical effectiveness of the fusion method in reducing velocity-retrieval uncertainty. In practice, bare, stable zones around two representative glaciers in the study area (Yanong and Xirinongpu) are selected as uncertainty-evaluation sites to ensure comparability and reliability.

3.7 Spatiotemporal analysis of velocity series

To characterize the spatial pattern, intra-annual seasonality, and multi-year trends of glacier surface velocity in the Kangri Karpo region, we perform quantitative spatiotemporal analyses using the monthly fused velocity product for 2015–2024, constrained by the RGI 7.0 glacier mask.

Spatial dimension. (1) Aggregate all monthly rasters from 2015–2024 to compute a multi-year mean (2015–2024) velocity map and visualize regional spatial structure; (2) conduct pixel-level statistics at the single-glacier scale to depict

https://doi.org/10.5194/egusphere-2025-6357
Preprint. Discussion started: 29 January 2026

spatial heterogeneity among glaciers; (3) use glacier area, slope, and aspect as explanatory variables and evaluate their relationships with velocity via Pearson correlation.

Temporal dimension. (1) Extract monthly velocities and compute cross-year means for each calendar month to derive the intra-annual (climatological) cycle; (2) apply per-pixel linear regression within the study mask to estimate the 2015–2024 trend in velocity, quantifying the direction and magnitude at decadal scale (units: $m \cdot d^{-1} \cdot dec^{-1}$); (3) further analyze interannual trends for each month to identify the seasons of predominant acceleration or deceleration.

4 Results and discussion

4.1 Quality improvements from multi-source fusion

All fusion results obtained in this study are presented in Figures S1–S10 of the Supplementary Material. To intuitively illustrate quality changes before and after fusion, this study compares the fused results with the pre-fusion Landsat and Sentinel-2 velocity products separately. These two mainstream optical remote-sensing sources are widely used for glacier velocity retrieval but suffer from limitations such as long revisit intervals and strong cloud interference. By contrasting with these primary inputs, we can determine whether the fusion method effectively integrates their strengths while mitigating the deficiencies of the original observations. On this basis, this subsection conducts comparative analyses from three perspectives—spatial completeness, temporal availability, and image smoothness—to comprehensively evaluate the performance of multi-source fusion in improving glacier velocity images.

https://doi.org/10.5194/egusphere-2025-6357
Preprint. Discussion started: 29 January 2026

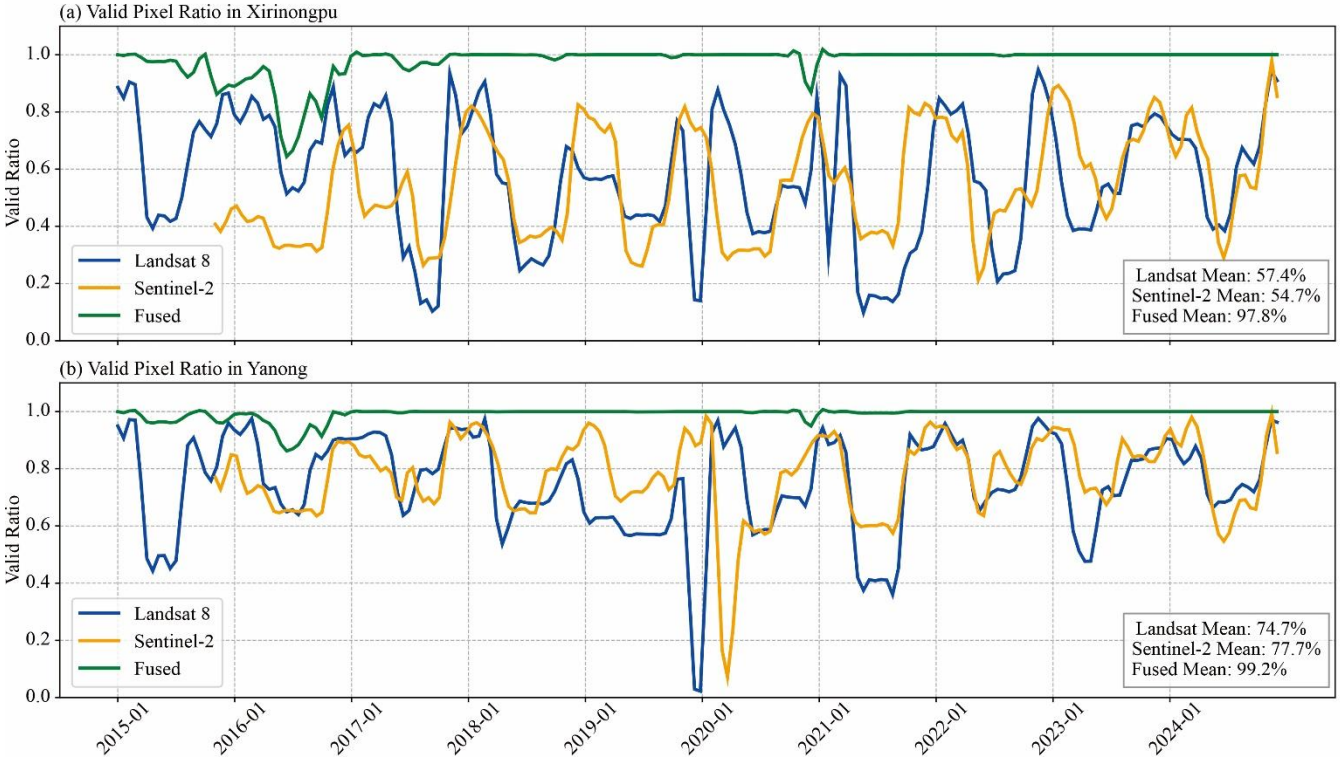

Figure 3: (a) Xirinongpu Glacier; (b) Yanong Glacier — proportion of valid pixels before and after fusion.

Figure 3 presents the monthly fraction of valid pixels in velocity images from 2015–2024 for the two representative glaciers, Xirinongpu and Yanong. The results show that, in most months, the fused product attains a substantially higher valid-pixel ratio than either single-source dataset. Over Xirinongpu, the mean valid-pixel ratios for Landsat and Sentinel-2 are 57.4% and 54.7%, respectively, whereas the fused result reaches 97.9%, an improvement of about 70%. Over Yanong, Landsat and Sentinel-2 achieve 74.7% and 77.1%, while the fused image further increases to 99.2%, an improvement of about 30%. These findings indicate that the proposed fusion method effectively overcomes the limitations of individual sources and markedly enhances data availability and continuity.

https://doi.org/10.5194/egusphere-2025-6357
Preprint. Discussion started: 29 January 2026

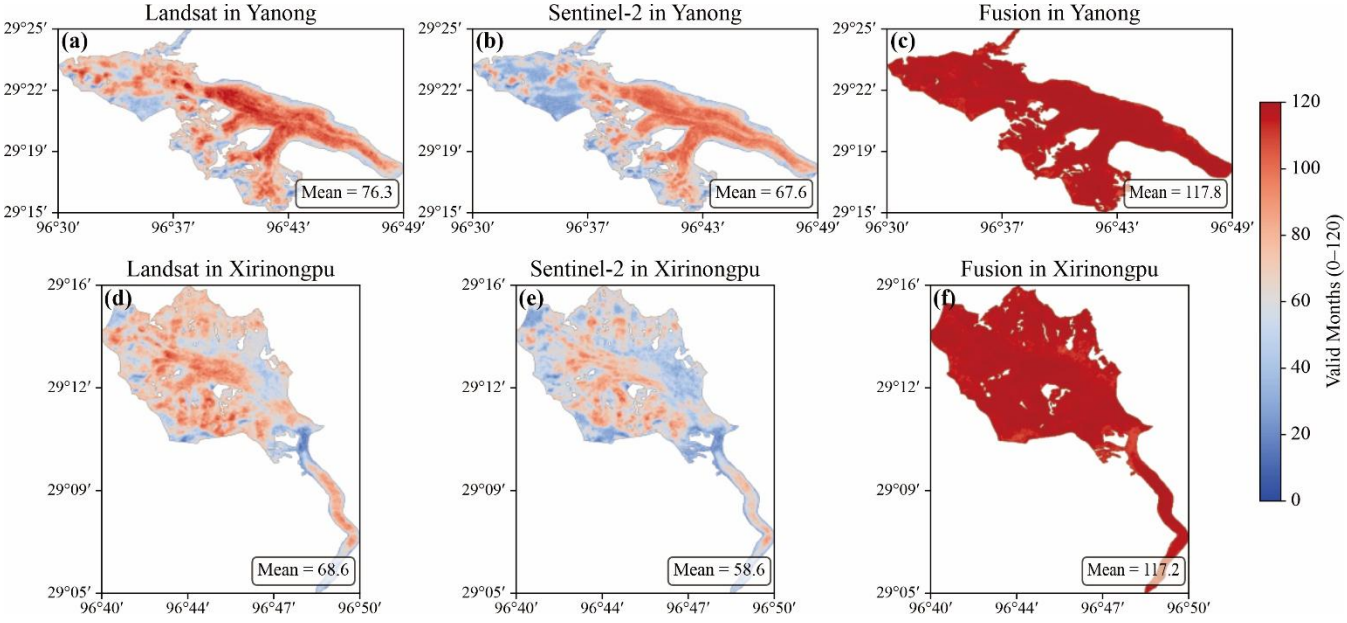

Figure 4: (a–c) Landsat / Sentinel-2 / fused velocity results: number of valid months on the Yanong Glacier; (d–f) Landsat / Sentinel-2 / fused velocity results: number of valid months on the Xirinongpu Glacier.

Figure 4 shows the spatial distribution of valid observation months before and after fusion over the representative Yanong and Xirinongpu glaciers. The fused product achieves near-complete temporal coverage in both areas: the vast majority of pixels have a full set of 120 monthly velocity values over the decade. For Yanong, the fused mean number of valid months is 117.8, compared with 76.3 for Landsat and 67.6 for Sentinel-2. For Xirinongpu, the fused mean reaches 117.2, versus 68.6 (Landsat) and 58.6 (Sentinel-2). Overall, the fusion method delivers substantial improvements in temporal availability.

https://doi.org/10.5194/egusphere-2025-6357
Preprint. Discussion started: 29 January 2026

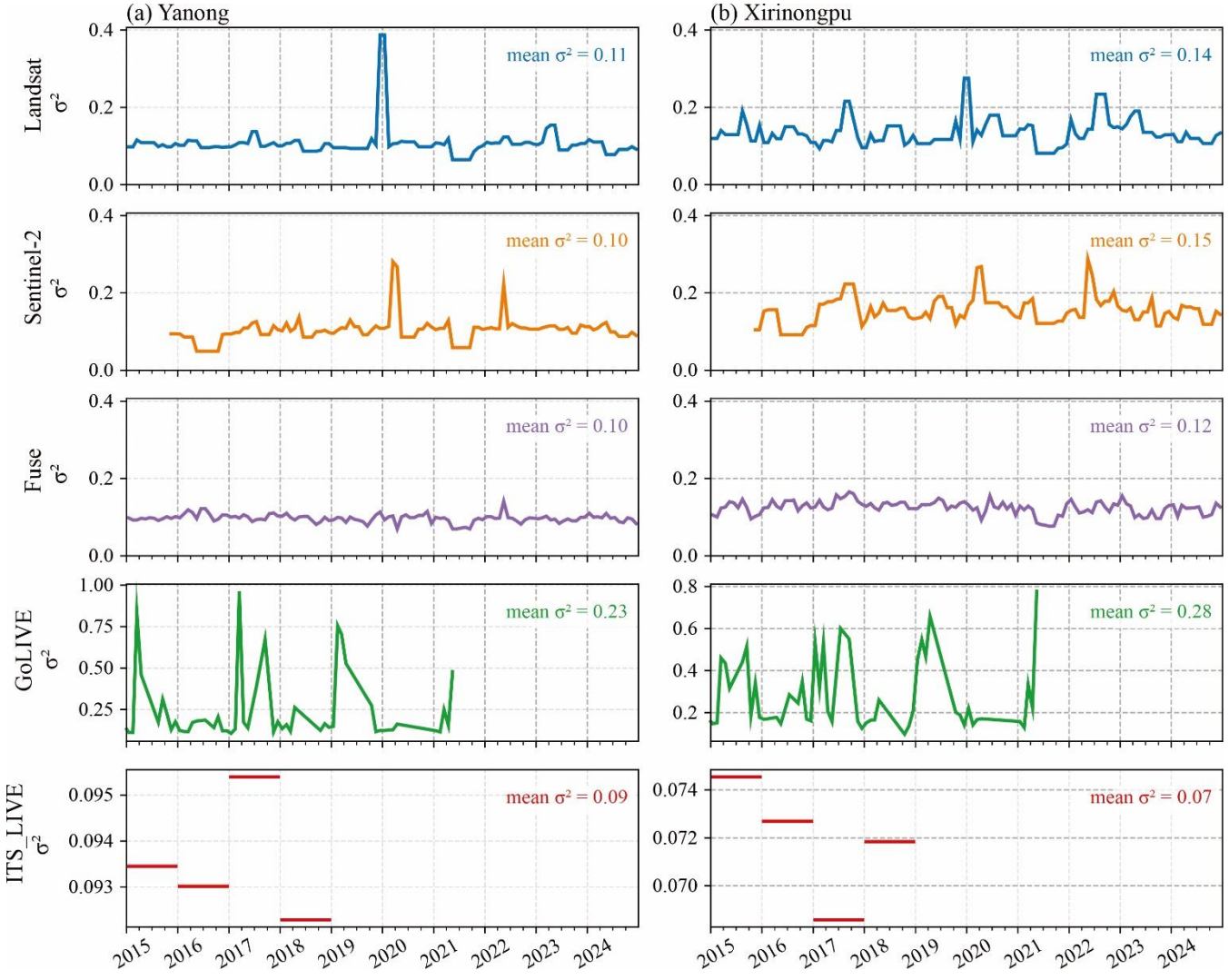

Figure 5: (a) Yanong Glacier; (b) Xirinongpu Glacier — variance of the Landsat velocity results, Sentinel-2 velocity results, fused results, GoLIVE dataset, and ITS_LIVE dataset.

Figure 5 shows the month-by-month spatial variance of velocity images during 2015–2024 for Yanong (Figure 5a) and Xirinongpu (Figure 5b), as an indicator of spatial smoothness. The curves compare Landsat, Sentinel-2, the fused product (Fusion), and the external datasets GoLIVE and ITS_LIVE.

Overall, the fused product exhibits a more stable, continuous, and low-fluctuation variance curve in both areas, indicating effective suppression of local noise and improved image consistency. At Yanong, the fused mean variance is 0.10-lower than GoLIVE (0.23), comparable to Sentinel-2 (0.10), and lower than Landsat (0.11). At Xirinongpu, the fused mean variance is 0.12, below Landsat (0.14) and Sentinel-2 (0.15), and also better than GoLIVE (0.28). Moreover, relative to the

https://doi.org/10.5194/egusphere-2025-6357
Preprint. Discussion started: 29 January 2026

two pre-fusion optical products, the fused series shows markedly reduced variance fluctuations, indicating greater smoothness and stability.

In sum, the proposed multi-source fusion not only enhances spatial completeness and temporal continuity, but also yields smoother spatial structure, providing a more stable and reliable velocity basis for subsequent spatiotemporal modeling and change detection.

4.2 Uncertainty analysis

Figure 6 presents the temporal evolution of monthly velocity-uncertainty estimates in stable areas for Landsat, Sentinel-2, the fused product, GoLIVE, and ITS_LIVE. The fused product's E_{off} remains consistently low with relatively steady fluctuations; its mean uncertainty is 0.05 m·d⁻¹, markedly below the glacier-wide mean velocities and better than the pre-fusion Landsat (0.07 m·d⁻¹) and Sentinel-2 (0.06 m·d⁻¹) results, substantially lower than GoLIVE (0.32 m·d⁻¹), and slightly higher than the annual-scale ITS_LIVE (0.03 m·d⁻¹). Overall, the proposed multi-source fusion performs well not only in spatial completeness and continuity but also in uncertainty within stable zones, indicating strong practical utility and potential for broader application.

https://doi.org/10.5194/egusphere-2025-6357
Preprint. Discussion started: 29 January 2026

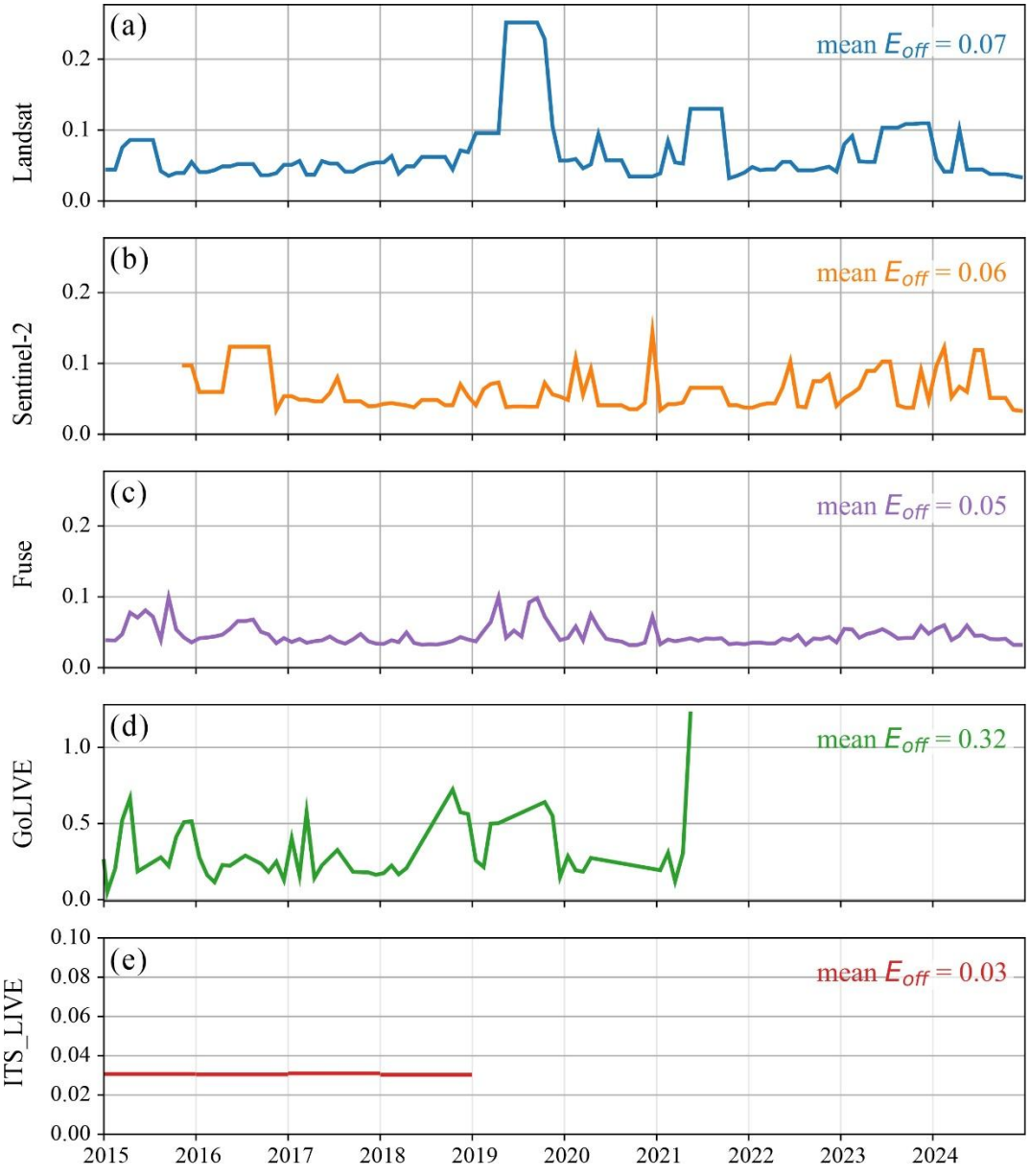

Figure 6: (a) Landsat velocity uncertainty; (b) Sentinel-2 velocity uncertainty; (c) Fused velocity uncertainty; (d) GoLIVE dataset uncertainty; (e) ITS_LIVE dataset uncertainty.

4.3 Spatial patterns of glacier surface velocity and controlling factors

From 2015 to 2024, glacier surface velocity in the Kangri Karpo region shows the canonical “fast center, slow margins” spatial pattern (Figure 7), with annual-mean maxima concentrated near the equilibrium line. The spatial organization of

https://doi.org/10.5194/egusphere-2025-6357
Preprint. Discussion started: 29 January 2026

335 velocity is closely tied to glacier morphology. To identify the primary controls, we analyze glacier attributes-size (area), slope, and aspect-using correlation analysis, centerline profiles, and cluster-based grouping to assess their roles in shaping glacier dynamics.

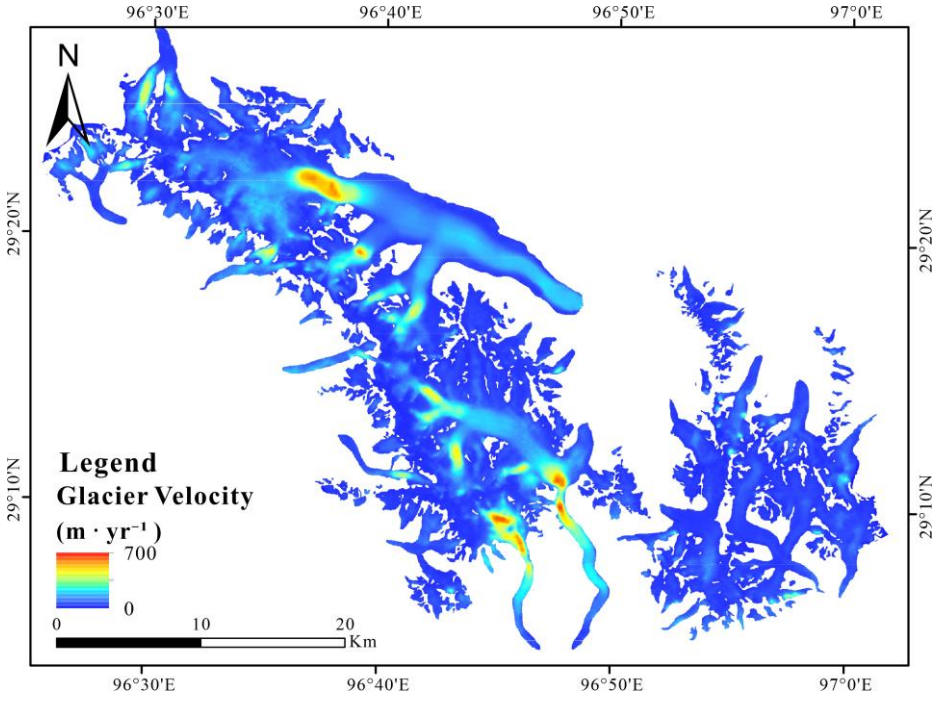

340 **Figure 7: Mean glacier surface velocity in the Kangri Karpo region (2015–2024).**

To examine how glacier size affects surface velocity in the Kangri Karpo region, we used total glacier area (km²) as the independent variable and the decadal mean surface velocity (m·yr⁻¹) as the dependent variable, and performed a correlation analysis on log-transformed variables. As shown in Figure 8, glacier area and mean surface velocity exhibit a moderate 345 positive correlation (Pearson r = 0.53, $p < 0.05$), indicating a statistically significant tendency for velocity to increase with area. The presence of outliers suggests that factors beyond area—such as slope and aspect—also influence glacier speed.

https://doi.org/10.5194/egusphere-2025-6357
Preprint. Discussion started: 29 January 2026

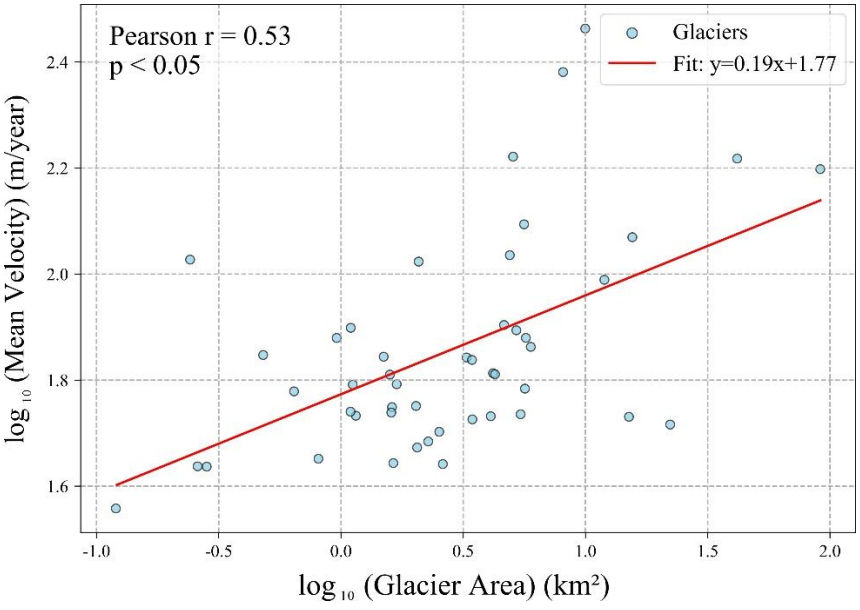

Figure 8: Correlation between glacier area and velocity. Blue points denote glaciers in the study area; the red solid line is the fitted regression; axes are logarithmic.

To further assess the role of slope, we conducted a pixel-level slope–velocity analysis along the main centerlines of two representative glaciers, Yanong and Xirinongpu (see Figure 9).

Compared with regional mixed analyses, the centerline approach effectively controls for differences in glacier size, morphology, and aspect, helping reveal the intrinsic slope–velocity relationship within a single glacier. Along the Yanong centerline (0–23,000 m), both velocity and slope show phased rises and falls, with marked co-variation in several segments. Scatterplot regression indicates a significant positive correlation between slope and surface velocity (Pearson r = 0.68, $p < 0.05$). Xirinongpu exhibits similar behavior, with a correlation of r = 0.63 ($p < 0.05$); the fitted linear model has a slope coefficient of 15.42 and an intercept of 153.3. These results pass significance tests and suggest that, within an individual glacier, increasing slope promotes higher surface velocity, consistent with glacier-flow theory: a steeper centerline increases the downslope gravitational component, enhancing basal sliding and viscous deformation and thereby accelerating flow.

https://doi.org/10.5194/egusphere-2025-6357
Preprint. Discussion started: 29 January 2026

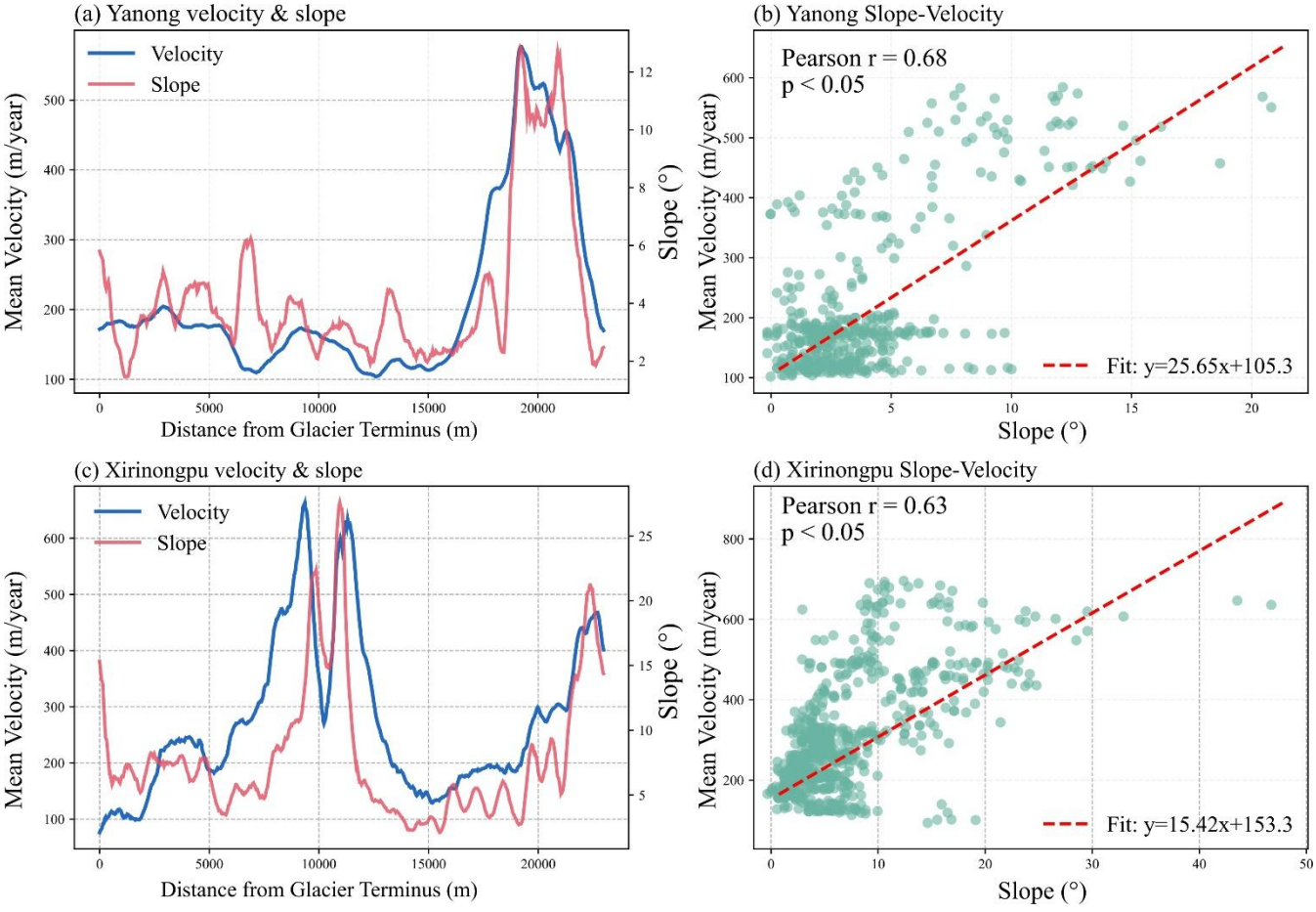

Figure 9: (a), (c) Variations of glacier surface velocity and slope along the centerlines of the Yanong and Xirinongpu glaciers. Blue curve: velocity; red curve: slope. (b), (d) Scatterplots of velocity versus slope for all pixels within the Yanong and Xirinongpu glacier masks; red dashed line: linear fit of the slope-velocity relationship.

To systematically examine the relationship between surface velocity and aspect across the Kangri Karpo glaciers, we first grouped major glaciers by morphological attributes (e.g., area and slope) using k-means clustering (Figure 10a). Clustering serves to control the confounding effects of area and slope when analyzing aspect–velocity links. The glaciers were partitioned into three clusters; because Cluster 3 contains only two glaciers and lacks statistical power, subsequent analyses focus on Clusters 1 and 2.

Building on aspect-based grouping, we summarized glacier surface velocities across aspect classes. As shown in Figure 10b,c, mean velocities differ by aspect (N, E, S, W), with both Cluster 1 and Cluster 2 exhibiting systematically higher velocities on south-facing S glaciers, and lower velocities on north-, east-, and west-facing glaciers. This pattern is consistent with the southeastern Tibetan Plateau's monsoonal climate: during summer, warm–moist air masses from the south enhance snowfall and meltwater supply on S-facing glaciers, favoring accumulation and flow. Stronger insolation on S-facing slopes

https://doi.org/10.5194/egusphere-2025-6357
Preprint. Discussion started: 29 January 2026

also increases surface energy input, promoting basal or surface melt and further accelerating flow. By contrast, N/E/W aspects receive less moisture and energy due to shading and airflow blocking, yielding lower velocities. These features highlight the coupled control of regional climate and topography on glacier motion.

In sum, glacier surface velocity in the Kangri Karpo region reflects the combined influence of multiple topographic factors. Statistically, glacier area is positively correlated with mean surface velocity, implying faster flow for larger glaciers. Centerline analyses further confirm the key regulatory role of slope within individual glaciers. Aspect-based results after clustering show that, under Indian monsoon influence, S-facing glaciers move significantly faster than other aspects, revealing the joint effects of regional climate and terrain. Overall, glacier size, slope, and aspect jointly shape the spatial pattern of surface velocity and are key determinants for understanding dynamical change on the Plateau.

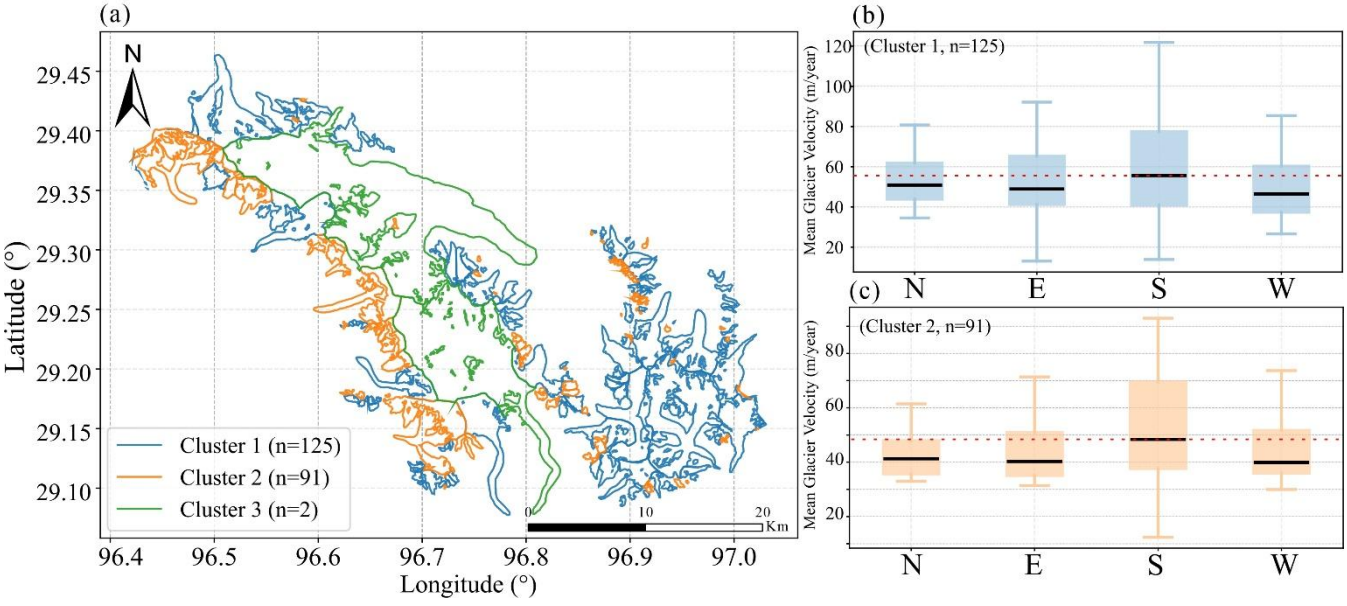

Figure 10: (a) K-means clustering (K = 3) of all glaciers in the study area based on area and slope. (b), (c) Boxplots of velocity by aspect for glaciers in Cluster 1 and Cluster 2, respectively. The box top is the upper quartile, the black line is the median, and the box bottom is the lower quartile; the red dashed line marks the median velocity of the aspect with the highest median.

4.4 Intra-annual variability of glacier surface velocity

To examine intra-annual variability in the Kangri Karpo region, we extracted monthly velocities from the 2015–2024 fused product and averaged each calendar month across years to obtain a typical annual cycle (Figure 11). The series shows clear seasonality: velocities are relatively low in January-March, rise from March, reach a first peak in May, remain comparatively steady, attain a second peak in October, and then decline-yielding a bimodal pattern. This bimodality accords

https://doi.org/10.5194/egusphere-2025-6357
Preprint. Discussion started: 29 January 2026

with the subglacial hydrology–dynamics framework for maritime glaciers: early in the melt season, meltwater and rainfall rapidly reach the bed via fractures; a high-storage, low-efficiency distributed system enhances basal sliding; by midsummer, sustained high discharge promotes channelization, lowering mean water pressure and reducing speed; toward the end of the melt season, partial re-closure can trigger a secondary autumn peak.

The standard-deviation envelope likewise indicates differing interannual variability by month. April-May-when acceleration initiates-exhibit larger standard deviations, implying greater year-to-year instability in the onset, magnitude, and duration of acceleration, likely influenced by contemporaneous air temperature, precipitation, and snow cover. In contrast, June through the following March is comparatively stable, with smaller fluctuations.

Overall, the "winter slowdown—summer acceleration" regime indicates a clear seasonal response of glacier surface velocity in the Kangri Karpo region.

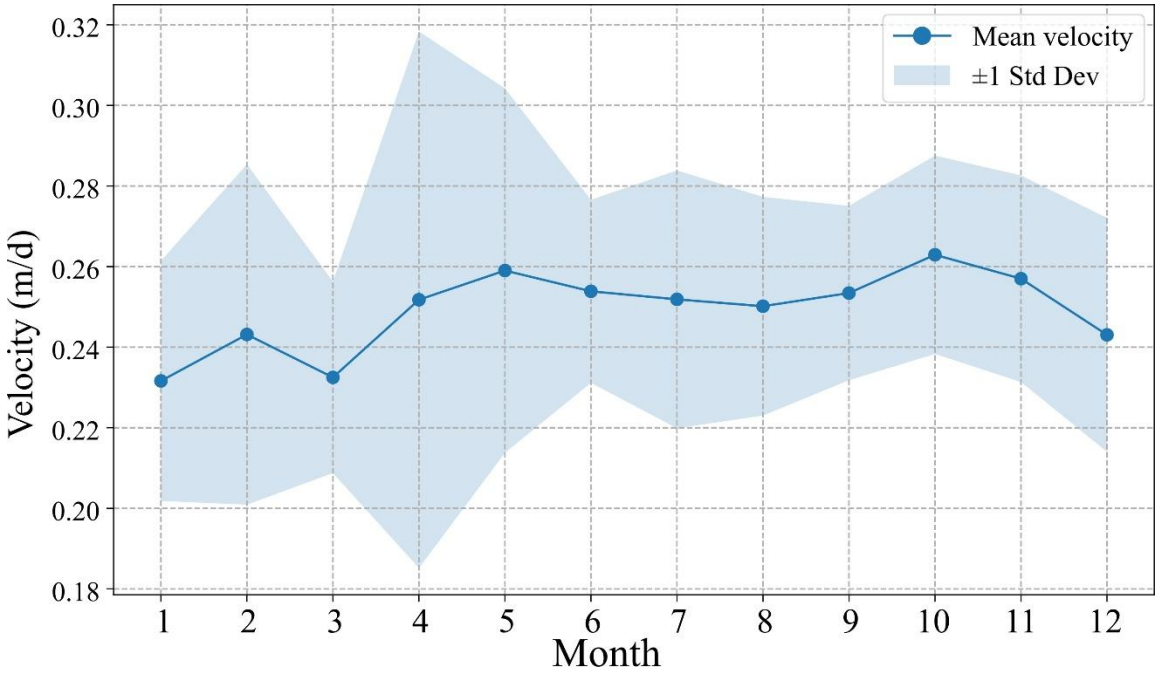

Figure 11: Monthly mean velocity (2015–2024). Blue points and line indicate the monthly means and their variation; blue shading shows ±1 standard deviation.

https://doi.org/10.5194/egusphere-2025-6357
Preprint. Discussion started: 29 January 2026

4.5 Interannual variability and long term trends

Using the monthly fused glacier-velocity images for 2015–2024, we applied linear regression to each pixel within the study mask in the Kangri Karpo region to quantify velocity trends (units: $m \cdot d^{-1} \cdot dec^{-1}$), thereby revealing the direction and magnitude of decadal changes in glacier surface speed (Figure 12).

The results show pronounced differences in decadal trends among major glaciers. On the two largest—Yanong and Xirinongpu—broad swaths of negative trends (blue boxes in Figure 12) indicate significant slowdowns, whereas the Yanong terminus exhibits marked acceleration, likely related to the influence of a proglacial lake. By contrast, smaller glaciers in the region (red boxes) display relatively clear acceleration.

Area-based statistics of the trend map (Figure 12) approximate a normal distribution, with most pixels falling between -0.1 and $+0.1$ $m \cdot d^{-1} \cdot dec^{-1}$, implying generally modest changes. The median trend is slightly positive, indicating a weak, basin-wide acceleration during 2015–2024.

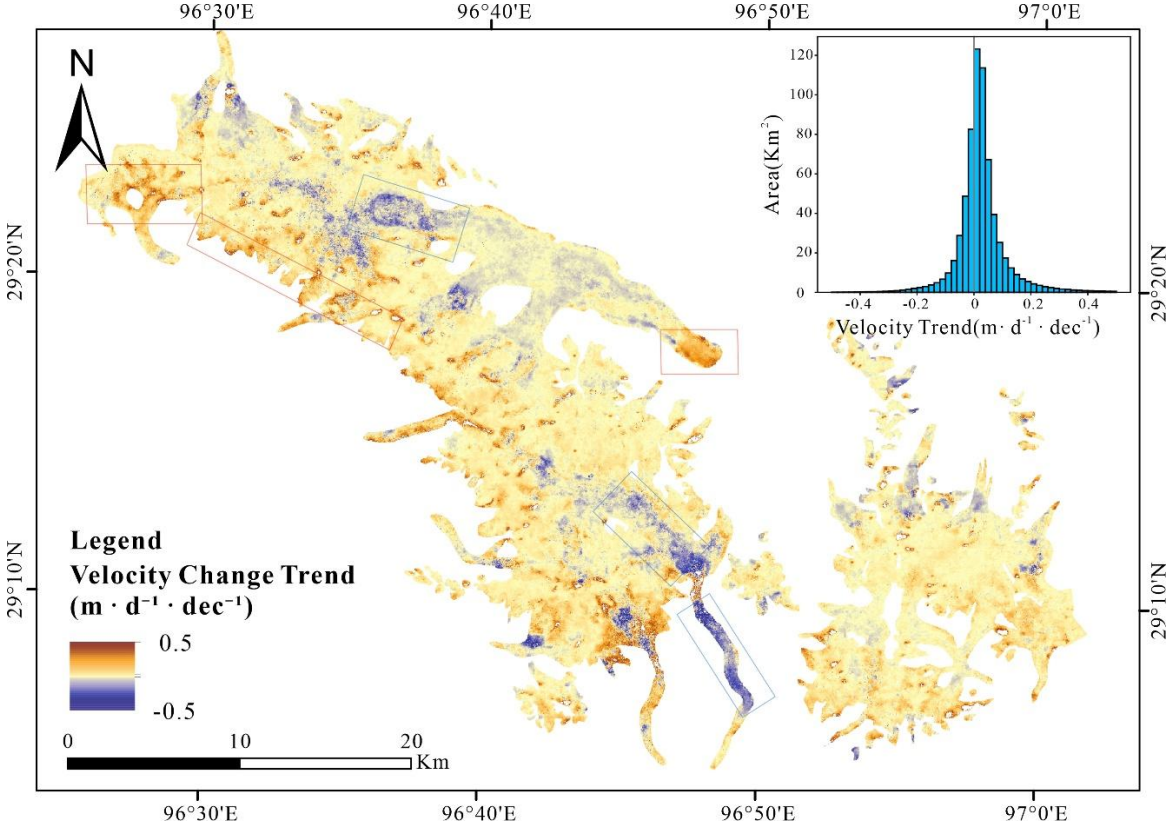

Figure 12: Main panel: per-pixel decadal trend in glacier surface velocity within the study mask (units: $m \cdot d^{-1} \cdot dec^{-1}$). Warmer (redder) colors indicate stronger acceleration; cooler (bluer) colors indicate stronger deceleration. Red and blue boxes highlight representative accelerating and decelerating areas. Upper-right inset: area-weighted distribution of trend values.

https://doi.org/10.5194/egusphere-2025-6357
Preprint. Discussion started: 29 January 2026

To further characterize interannual variability, we applied linear regression to the 2015–2024 velocity series and summarized each glacier's(> 1 km²) trend together with its mean aspect. Figure 13 presents the multi-year trends of glacier surface velocity and the distribution of mean aspects across the Kangri Karpo region.

Spatially, accelerating and decelerating glaciers show distinct patterns. Some accelerating glaciers are concentrated in the western and central sectors of the region, whereas decelerating glaciers are relatively clustered in the eastern sector and parts of the central area. Accelerating glaciers predominantly exhibit a southwest–northeast principal flow orientation, while decelerating glaciers are more clearly aligned east–west, indicating differences in multi-year trends by flow orientation.

The three bar charts on the right further summarize change characteristics by glacier type. Trend-class distributions show that ~38.3% of glaciers exhibit significant acceleration, 25.5% show significant deceleration, and 36.2% have no significant multi-year trend ($p \geqslant 0.05$). By mean aspect, significantly accelerating glaciers are concentrated on south-facing (50.0%) and west-facing (27.8%) slopes, whereas significantly decelerating glaciers are dominated by east-facing (58.3%) and north-facing (25.0%) slopes. These results indicate clear directional differences in recent glacier dynamics, likely governed by a combination of regional topography, snow/ice supply, and climatic conditions. In sum, the multi-year velocity trends and principal flow orientations of Kangri Karpo glaciers exhibit spatial heterogeneity and directional structure, and the underlying mechanisms of glacier response to climate forcing in the southeastern Tibetan Plateau require further analysis.

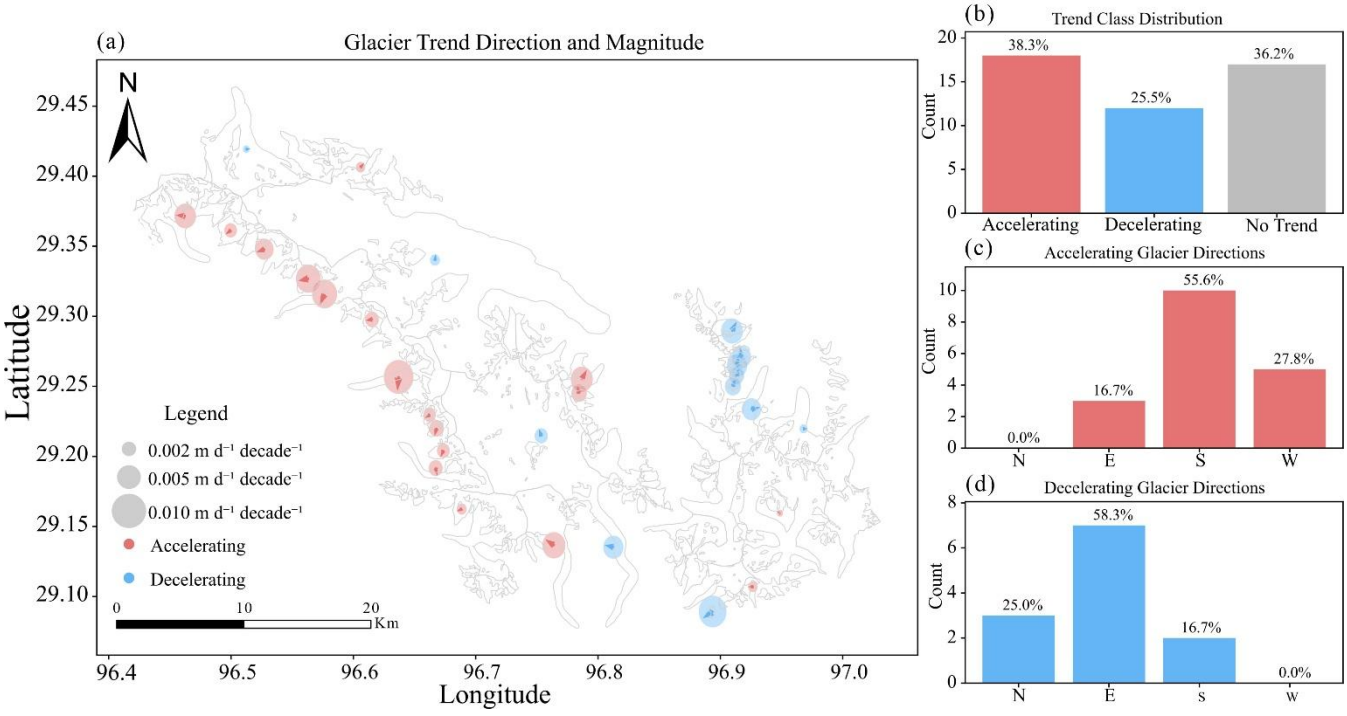

Figure 13: (a) Schematic map of glacier velocity trends across the study area. Circle color indicates trend direction (acceleration/deceleration); circle size indicates trend magnitude; the arrow inside each circle shows the glacier's mean aspect. Glaciers without circles exhibit no significant trend. (b) Counts and percentages of glaciers by trend class (significant acceleration /

https://doi.org/10.5194/egusphere-2025-6357
Preprint. Discussion started: 29 January 2026

significant deceleration / no significant change). (c) Counts and percentages of significantly accelerating glaciers by aspect. (d) Counts and percentages of significantly decelerating glaciers by aspect.

Figure 14 further presents monthly multi-year velocity trends (2015–2024) and their 95% confidence intervals for different glacier types in the Kangri Karpo region: the upper panel shows significantly accelerating glaciers by month, and the lower panel shows significantly decelerating glaciers by month. The y-axis is the decadal trend in velocity (m d^{-1} $decade^{-1}$). Line segments above the bars indicate the 95% confidence interval of the monthly mean trend.

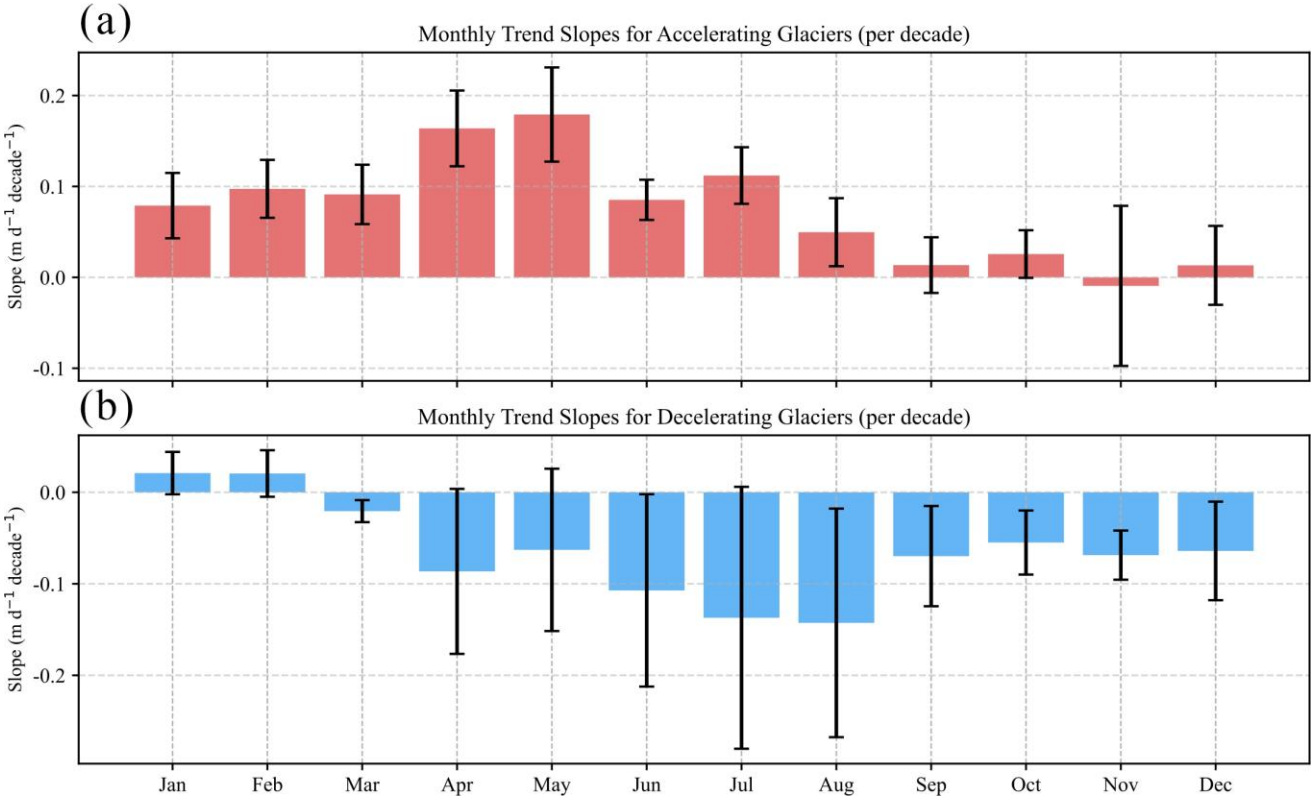

Figure 14: (a), (b) Monthly velocity trends for significantly accelerating/decelerating glaciers; black lines above the bars indicate the 95% confidence interval of the monthly mean trend.

From the accelerating-glacier subset, acceleration concentrates in late spring to early summer: April and May exhibit the largest multi-year trends (~0.15–0.20 m d^{-1} $decade^{-1}$), with confidence intervals excluding zero, indicating strong significance. A plausible explanation is the recent advance of the melt season in southeastern Tibet (Li et al., 2025; Wu et al., 2022), during which a distributed subglacial drainage system has high storage and low efficiency, elevating basal water pressure and enabling earlier meltwater access to the bed—thus promoting early-season acceleration.

https://doi.org/10.5194/egusphere-2025-6357
Preprint. Discussion started: 29 January 2026

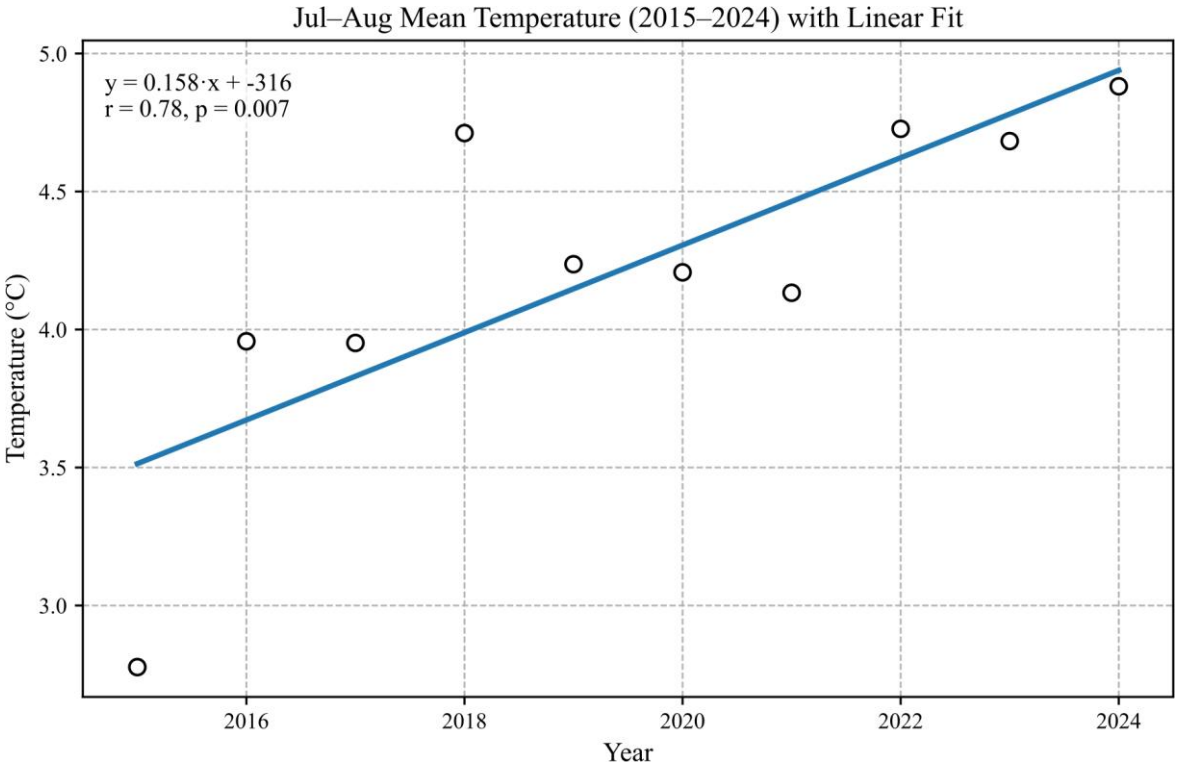

Figure 15: ERA5-Land temperature trends for July and August, 2015–2024. Circles denote each year's mean temperature; the blue solid line is the linear fit.

For decelerating glaciers, slowdown concentrates in summer—especially July–August—when trends fall below −0.15 m d^{-1} $decade^{-1}$, indicating the strongest deceleration. A plausible cause is the marked rise in July–August air temperature (ERA5-Land), which intensifies mass loss, while the subglacial drainage system is channelized and efficient; glacier motion is then dominated by creep, so negative mass balance drives a pronounced deceleration peak in July–August.

By size, accelerating glaciers are generally smaller. Because creep is weaker in small glaciers, early-season hydrological acceleration can outweigh the year-scale mass deficit, making acceleration more common. Large glaciers are more strongly governed by creep, with mass balance the primary control on speed; hence they tend to decelerate in summer and over multi-year scales, consistent with the warming-driven, widespread slowdown across High Mountain Asia (Dehecq et al., 2019).

In summary, the "April–May acceleration vs. July–August deceleration" pattern reflects the joint effects of an advanced melt season (hydrological forcing) and mass balance. This broadly accords with current understanding, while highlighting that for some glaciers, early-season meltwater acceleration can exceed the decelerating influence of mass loss.

https://doi.org/10.5194/egusphere-2025-6357
Preprint. Discussion started: 29 January 2026

4.6 Limitations and future directions

The UAV survey in this study covers only the glacier tongue, and fusion weights are primarily calibrated from a limited UAV reference area at the Yanong Glacier terminus, constraining their spatial and temporal transferability. In addition, differences in sensor revisit cycles (Landsat ≈ 16 d; Sentinel-1 ≈ 12 d; Sentinel-2 ≈ 10 d) preclude strict month-to-month alignment, producing baseline-length mismatches and temporal smoothing that inevitably introduce velocity-estimation biases. Together, these factors bound the achievable accuracy of monthly glacier-velocity retrievals.

Future work can proceed along two lines: (i) introduce spatiotemporally adaptive weighting—via stratified calibration or modeling conditioned on topography, surface texture, and acquisition geometry—to improve applicability over larger areas and longer periods; and (ii) standardize or assimilate time intervals by mapping multi-sensor displacements/velocities to a "standard month" framework to reduce baseline-induced biases. With higher-resolution, higher-cadence observations continuing to emerge, these refinements should substantially enhance the method's generalizability and support broader multi-sensor fusion.

5 Conclusions

This study proposes and implements a high-resolution glacier surface-velocity retrieval method based on multi-sensor data fusion, and produces monthly velocity products for the Kangri Karpo region for 2015–2024. Relative to existing large-area public datasets, our products markedly improve spatial resolution and enhance the detectability of small mountain glaciers. Compared with single-sensor inputs prior to fusion, the fused results increase the proportion of valid pixels by ~50%, add ~50 valid months per pixel over the decade, and improve spatial smoothness—demonstrating that the method effectively mitigates single-source limitations under complex mountain conditions.

In spatial terms, glacier surface velocity during 2015–2024 exhibits the canonical "fast center, slow margins" pattern: multi-year mean maxima exceed 700 $m \cdot yr^{-1}$, whereas values in lower reaches and most tributaries are generally <100 $m \cdot yr^{-1}$. Regarding attribute controls, Pearson correlations indicate significant relationships between velocity and glacier area, slope, and aspect: larger glaciers tend to flow faster; within individual glaciers, velocity correlates more strongly with slope; after controlling for area and slope, south-facing glaciers are slightly faster than other aspects.

Seasonally, the series shows a clear cycle: peaks occur near the onset and end of the melt season, with persistently elevated speeds throughout the melt period. Interannually, most pixelwise decadal trends fall within −0.1 to +0.1 $m \cdot d^{-1} \cdot dec^{-1}$, indicating generally modest changes; the median trend is slightly positive, implying weak regional acceleration during 2015–2024. By significance class, ~38.3% of glaciers accelerate significantly, 25.5% decelerate significantly, and 36.2% show no significant trend ($p \geqslant 0.05$). By aspect, significant acceleration is concentrated on south- (50.0%) and west-facing (27.8%) glaciers, whereas significant deceleration is dominated by east- (58.3%) and north-facing (25.0%) glaciers. Month-resolved interannual trends show acceleration mainly in April–May (~0.15–0.20 $m \cdot d^{-1} \cdot dec^{-1}$), likely reflecting earlier melt-season

https://doi.org/10.5194/egusphere-2025-6357
Preprint. Discussion started: 29 January 2026

onset and meltwater-driven speed-up; deceleration concentrates in July–August ($\leqslant -0.15$ m·d^{-1}·dec^{-1}), likely reflecting mass-loss-driven slow-down.

These spatiotemporal patterns likely reflect interactions among glacier mass balance, subglacial hydrologic evolution, and regional climate (e.g., monsoon forcing). However, the specific drivers merit further process-based analysis integrating mass-balance observations and hydro-climatic factors.

Data availability. Data will be made available on request.

Supplement. The supplement related to this article is available online at:

Author contributions. DG, KW and SL designed this study. YD, ZJ and DM carried out the field surveys. DG carried out the data processing. DG and KW wrote the article. KW, TB and CH edited every version of the article.

Competing interests. At least one of the (co-)authors is a member of the editorial board of The Cryosphere.

Acknowledgements. This work was supported by the National Key Research and Development Program of China (grant no. 2024YFF0810700), the National Natural Science Foundation of China (grant nos. 42571160 and 42361021), and the Natural Science Foundation of Yunnan (grant no. 202401AS070125).

References

Berthier, E., Vadon, H., Baratoux, D., and Arnaud, Y.: Surface motion of mountain glaciers derived from satellite optical imagery, Remote Sens. Environ., 95, 14–28, https://doi.org/10.1016/j.rse.2004.11.005, 2005.

Chen, H., Chen, Y., Li, W., and Li, Z.: Quantifying the contributions of snow/glacier meltwater to river runoff in the Tianshan Mountains, Central Asia, Glob. Planet. Change, 181, 102982, https://doi.org/10.1016/j.gloplacha.2019.01.002, 2019.

Fahnestock, M., Scambos, T., Moon, T., Gardner, A., Haran, T., and Klinger, M.: Rapid large-area mapping of ice flow using Landsat 8, Remote Sens. Environ., 185, 84–94, https://doi.org/10.1016/j.rse.2015.11.023, 2016.

Fan, J., Wang, Q., Liu, G., Zhang, L., Guo, Z., Tong, L., and Peng, J.: Monitoring and analyzing mountain glacier surface movement using SAR data and a terrestrial laser scanner: a case study of the Himalayas North Slope Glacier Area, Remote Sens., 11, 625, https://doi.org/10.3390/rs11060625, 2019.

Fountain, A. G., Campbell, J. L., and Schuur, E. A. G.: The disappearing cryosphere: impacts and ecosystem responses to rapid cryosphere loss, BioScience, 62, 405–415, https://doi.org/10.1525/bio.2012.62.4.11, 2012.

Fu, Y., Zhang, B., Liu, G., Zhang, R., and Liu, Q.: An optical flow SBAS technique for glacier surface velocity extraction using SAR images, IEEE Trans. Geosci. Remote Sens., 60, 1–15, https://ieeexplore.ieee.org/document/9863863, 2022.

https://doi.org/10.5194/egusphere-2025-6357
Preprint. Discussion started: 29 January 2026

Gardner, A. S., Moholdt, G., Scambos, T., Fahnstock, M., Ligtenberg, S., van den Broeke, M., and Nilsson, J.: Increased West Antarctic and unchanged East Antarctic ice discharge over the last 7 years, The Cryosphere, 12, 521–547, https://doi.org/10.5194/tc-12-521-2018, 2018.

Huang, L. and Li, Z.: Comparison of SAR and optical data in deriving glacier velocity with feature tracking, Int. J. Remote Sens., 32, 2481–2500, https://doi.org/10.1080/01431161003720395, 2011.

Huss, M. and Hock, R.: A new model for global glacier change and sea-level rise, Front. Earth Sci., 3, 54, https://doi.org/10.3389/feart.2015.00054, 2015.

Kääb, A., Huggel, C., Fischer, L., and Guex, S.: Remote sensing of glacier- and permafrost-related hazards in high mountains: an overview, Nat. Hazards Earth Syst. Sci., 5, 527–554, https://doi.org/10.5194/nhess-5-527-2005, 2005.

Lei, Y., Gardner, A., and Agram, P.: Autonomous repeat image feature tracking (autoRIFT) and its application for tracking ice displacement, Remote Sens., 13, 749, https://doi.org/10.3390/rs13040749, 2021.

Liu, S. Y., Wu, T. H., Wang, X., Wu, X. D., and Yao, X. J.: Changes in the global cryosphere and their impacts: a review and new perspective, Sci. Cold Arid Reg., 13, 1–12, https://doi.org/10.3724/SP.J.1226.2020.00343, 2021.

Luckman, A., Murray, T., Jiskoot, H., and Pritchard, H.: ERS SAR feature-tracking measurement of outlet glacier velocities on a regional scale in East Greenland, Ann. Glaciol., 37, 129–134, https://doi.org/10.3189/172756403781816428, 2003.

Luckman, A., Quincey, D., and Bevan, S.: The potential of satellite radar interferometry and feature tracking for monitoring flow rates of Himalayan glaciers, Remote Sens. Environ., 111, 172–181, https://doi.org/10.1016/j.rse.2007.05.016, 2007.

Maksymiuk, O., Mayer, C., and Stilla, U.: Velocity estimation of glaciers with physically-based spatial regularization—Experiments using satellite SAR intensity images, Remote Sens. Environ., 182, 283–296, https://doi.org/10.1016/j.rse.2015.11.007, 2016.

Mohanty, A., Srivastava, P. K., and Aggarwal, A.: Review of glacier velocity and facies characterization techniques using multi-sensor approach, Environ. Dev. Sustain., 27, 1–24, https://doi.org/10.1007/s10668-024-04604-7, 2025.

Nan, Y., Tian, F., McDonnell, J., Ni, G., Tian, L., and Li, Z.: Glacier meltwater has limited contributions to the total runoff in the major rivers draining the Tibetan Plateau, npj Clim. Atmos. Sci., 8, 1060–1073, https://doi.org/10.1038/s41612-025-01060-6, 2025.

Ren, J. W., Ye, B. S., Ding, Y. J., and Liu, S. Y.: Initial estimate of the contribution of cryospheric change in China to sea level rise, Chin. Sci. Bull., 56, 1375–1381, https://doi.org/10.1007/s11434-011-4474-3, 2011.

RGI Consortium: Randolph Glacier Inventory – A Dataset of Global Glacier Outlines: Version 7.0, NSIDC: National Snow and Ice Data Center, Boulder, Colorado, USA, https://doi.org/10.5067/F6JMOVY5NAVZ, 2023.

Scherler, D., Leprince, S., and Strecker, M. R.: Glacier-surface velocities in alpine terrain from optical satellite imagery—Accuracy improvement and quality assessment, Remote Sens. Environ., 112, 3806–3819, https://doi.org/10.1016/j.rse.2008.05.018 2008.

Slaymaker, O. and Kelly, R. E. J.: The Cryosphere and Global Environmental Change, Blackwell Publishing, Oxford, UK, ISBN 978-1-4051-2976-3, 2007.

https://doi.org/10.5194/egusphere-2025-6357
Preprint. Discussion started: 29 January 2026

Slemmons, K. E. H., Saros, J. E., and Simon, K.: The influence of glacial meltwater on alpine aquatic ecosystems: a review, Environ. Sci.: Processes Impacts, 15, 1794–1806, https://doi.org/10.1039/C3EM00243H, 2013.

Sun, Y., Jiang, L., Liu, L., Sun, Y., and Wang, H.: Spatial-temporal characteristics of glacier velocity in the Central Karakoram revealed with 1999–2003 Landsat-7 ETM+ Pan images, Remote Sens., 9, 1064, https://doi.org/10.3390/rs9101064, 2017.

Wang, Q., Fan, J., Zhou, W., Tong, L., and Guo, Z.: 3D surface velocity retrieval of mountain glacier using an offset tracking technique applied to ascending and descending SAR constellation data, Int. J. Digit. Earth, 12, 1145–1162, https://doi.org/10.1080/17538947.2018.1470690, 2019.

Wu, K., Liu, S., Jiang, Z., Xu, J., Wei, J., and Guo, W.: Recent glacier mass balance and area changes in the Kangri Karpo Mountains from DEMs and glacier inventories, The Cryosphere, 12, 103–121, https://doi.org/10.5194/tc-12-103-2018, 2018.

Wu, K., Liu, S., Xu, J., Zhu, Y., Liu, Q., Jiang, Z., and Wei, J.: Spatiotemporal variability of surface velocities of monsoon temperate glaciers in the Kangri Karpo Mountains, southeastern Tibetan Plateau, J. Glaciol., 67, 186–191, https://doi.org/10.1017/jog.2020.98, 2021.

Yan, S., Liu, G., Wang, Y., and Ruan, Z.: Accurate determination of glacier surface velocity fields with a DEM-assisted pixel-tracking technique from SAR imagery, Remote Sens., 7, 10898–10914, https://doi.org/10.3390/rs70810898, 2015.

Yang, B., Bräuning, A., Dong, Z., and Zhang, Z.: Late Holocene monsoonal temperate glacier fluctuations on the Tibetan Plateau, Glob. Planet. Change, 60, 126–140, https://doi.org/10.1016/j.gloplacha.2007.01.021, 2008.

Yao, R., Li, S., and Chen, D.: Runoff response to climate in two river basins supplied by small glacier meltwater in Southern and Northern Tibetan Plateau, Atmosphere, 14, 711, https://doi.org/10.3390/atmos14040711, 2023.

Ye, Q., Wang, Y., Liu, L., Guo, L., Zhang, X., Dai, L., and Zhai, L.: Remote sensing and modeling of the cryosphere in high mountain Asia: a multidisciplinary review, Remote Sens., 16, 1709, https://doi.org/10.3390/rs16101709, 2024.

Zemp, M., Huss, M., Thibert, E., Eckert, N., McNabb, R., Huber, J., Barandun, M., Machguth, H., Nussbaumer, S. U., Gärtner-Roer, I., Thomson, L., Paul, F., Maussion, F., Kutuzov, S., and Cogley, J. G.: Global glacier mass changes and their contributions to sea-level rise from 1961 to 2016, Nature, 568, 382–386, https://doi.org/10.1038/s41586-019-1071-0, 2019.

Zhang, Y., Hirabayashi, Y., Liu, Q., and Liu, S.: Glacier runoff and its impact in a highly glacierized catchment in the southeastern Tibetan Plateau: past and future trends, J. Glaciol., 61, 713–730, https://doi.org/10.3189/2015JoG14J188, 2015.

Zhang, Y., Liu, S., and Ding, Y.: Glacier meltwater and runoff modelling, Keqicar Baqi glacier, southwestern Tien Shan, China, J. Glaciol., 53, 91–98, https://doi.org/10.3189/172756507781833956, 2007.

Zhang, Y., Xu, C.-Y., Hao, Z., Zhang, L., Ju, Q., and Lai, X.: Variation of melt water and rainfall runoff and their impacts on streamflow changes during recent decades in two Tibetan Plateau basins, Water, 12, 3112, https://doi.org/10.3390/w12113112, 2020.

https://doi.org/10.5194/egusphere-2025-6357
Preprint. Discussion started: 29 January 2026

Zhou, J., Li, Z., and Guo, W.: Estimation and analysis of the surface velocity field of mountain glaciers in Muztag Ata using satellite SAR data, Environ. Earth Sci., 73, 5533–5545, https://doi.org/10.1007/s12665-013-2749-5, 2014.

Zongxing, L., Qi, F., Wang, Q. J., Song, Y., and Jianguo, L.: Quantitative evaluation on the influence from cryosphere meltwater on runoff in an inland river basin of China, Glob. Planet. Change, 146, 182–195, https://doi.org/10.1016/j.gloplacha.2016.06.005, 2016.